Bulletin of the Seismological Society of America, Vol. 99, No. 2B, pp. 1287–1301, May 2009, doi: 10.1785/0120080200

Seismic-Wave Strain, Rotation, and Gradiometry for the 4 March 2008 TAIGER Explosions

by Charles A. Langston, W. H. K. Lee, C. J. Lin, and C. C. Liu

Abstract Acceleration spatial gradients, horizontal strains, and horizontal rotation were computed using strong-motion array data from the 4 March 2008 TAIGER explosions in northeastern Taiwan and used in conjunction with the original three component acceleration data to perform a gradiometric analysis of the strong ground motion wave train. The analysis yields a complex, frequency-dependent view of the nature of seismic-wave propagation over short propagation distances that imply significant lateral velocity changes in structure. Areal strain and rotation about the vertical axis have equal amplitudes and suggest significant wave scattering within the confines of the river valley where the experiment was performed and/or significant departure from an axisymmetric explosion source. Gradiometry shows that the *P* wave arrives at the array 35° off-azimuth clockwise from the straight-line path and appears to have been refracted from the northern side of the valley. Large, slowly propagating secondary surface waves initially arrive 45° counterclockwise from the straight-line path but later arrivals are seen to propagate in all directions, including back toward the explosion source. A frequency-dependent radiation pattern for the triple-borehole explosion in comparison to the single-borehole explosion explains the differences in the maximum amplitudes between the sources seen in the acceleration data. The use of seismic strain and rotation with standard particle motion wave fields at a single location allows for a direct view of seismic-wave propagation that illuminates the true nature of the seismogram.

Introduction

Since the late nineteenth century, ground motions have been measured using basically the same conventional method. Although the quality and numbers of sensors and recording devices have improved dramatically over time, seismometry has generally concentrated on the measurement of vector particle motion at a single point within the Earth. The mysteries of seismograms have generally been unraveled through application of wave propagation models and empirical data collection efforts that build on past experience (e.g., Aki and Richards, 1980). Although seismograms of particle motions can give clues about the types of seismic waves that may be observed, it is remarkable that the field has not developed more widespread methods to directly measure attributes of seismic waves other than their simple effect in being able to move a point in the ground.

It would be very useful to have direct measurements of wave speed, direction, spatial amplitude variations, stress, strain, and rotation to decipher the physical state and heterogeneity of the Earth's continuum. Such wave measurements would also make it much easier to gain a deeper understanding of the seismic-wave field over the entire duration of a seismogram. Of course, specialized dense arrays of seismic instruments are used in refraction and reflection seismology for inferring Earth structure at all scales and also in verification seismology for detecting and locating distant seismic events (e.g., Havskov and Alguacil, 2004). These arrays are made up of many standard seismic instruments and are quite successful in measuring wave speeds and directions. Even so, imagine how much easier it would be to understand a seismogram and all of its constitutive waves if there were direct observations of wave attributes, such as strain, rotation, and directional amplitude changes, in addition to wave speed and direction. Wave types could be inferred from dilatation and curl fields (e.g., Aki and Richards, 1980), directional amplitude changes could discriminate between different seismic phases and infer their propagation characteristics (Langston, 2007a), wave speeds can help identify seismic phases and infer medium properties, and, obviously, wave direction can be used to infer source position or scattering properties of the medium. Direct observations of this kind would be invaluable for inferring whether data are appropriate for the assumptions of a particular modeling or imaging theory.

The purpose of this report is to present an analysis of strong ground motion data from two explosion sources deto-

nated for the TAIGER (Taiwan Integrated GEodynamics Research) project in Taiwan on 4 March 2008 (Lin *et al.*, 2009) using recently developed techniques of seismic-wave gradiometry in addition to computing geodetic strain and rotation (Langston, 2007a,b,c; Langston and Liang, 2008). Seismic-wave gradiometry is a technique that utilizes the wave spatial gradients (strains and rotations) and wave particle motions to directly determine the wave attributes mentioned previously. In a sense, it is a tool to illuminate waves within the seismogram using observations obtained at essentially one point within the Earth. There is nothing particularly special about these explosions or the geographical location of the seismic observations except for the fact that the array used for recording the close-in accelerations was designed purposefully as a seismic gradiometer. That is, the symmetry of the array and station spacing was constructed so that it would sample less than 10% of target seismic-wave wavelengths and that data from each station could be used in a spatial finite difference scheme to calculate geodetic, time-dependent seismic strains and rotations (Spudich *et al.*, 1995; Langston and Liang, 2008; Lin *et al.*, 2009). Indeed, one of the main purposes of the gradiometer was to compare array-determined seismic rotations with rotations measured directly with broadband rotation meters (Lin *et al.*, 2009).

In this report, we use the gradiometer data to understand the seismic-wave field from a purist's point of view by asking a series of fundamental questions. What information does gradiometry yield that would be useful in understanding the explosion sources? What information is there that indicates how waves propagate within the river valley where the gradiometer and borehole explosion sources were emplaced? Is the design of the gradiometer adequate to the task? Is gradiometry a useful and practical technique for illuminating the wave field? We show that it is possible to construct a high-quality gradiometer from standard accelerographs that accurately measures the seismic-wave field. We also show that it is surprising how complex the wave field can become even at short distances from the source. As a technique, gradiometry goes a long way toward fulfilling the goal of making fundamentally new, and direct, observations of seismic waves over simple modeling of particle motions.

Data

Lin *et al.* (2009) present the source parameters of the two large TAIGER explosions and details concerning the construction of the close-in accelerograph network and gradiometer. Figure 1 summarizes the geometry of the sources and the gradiometer that are considered in this article. Two other strong-motion stations, one at about 250 m from the source and the other at about 600 m, also recorded the explosions but are not used here. The N3P explosion consisted of three boreholes filled with about 1000 kg of explosives each that were simultaneously detonated at 17:01 UTC. A 750 kg, single-borehole shot (N3) was detonated an hour later at 18:01 UTC. The gradiometer array and explosion

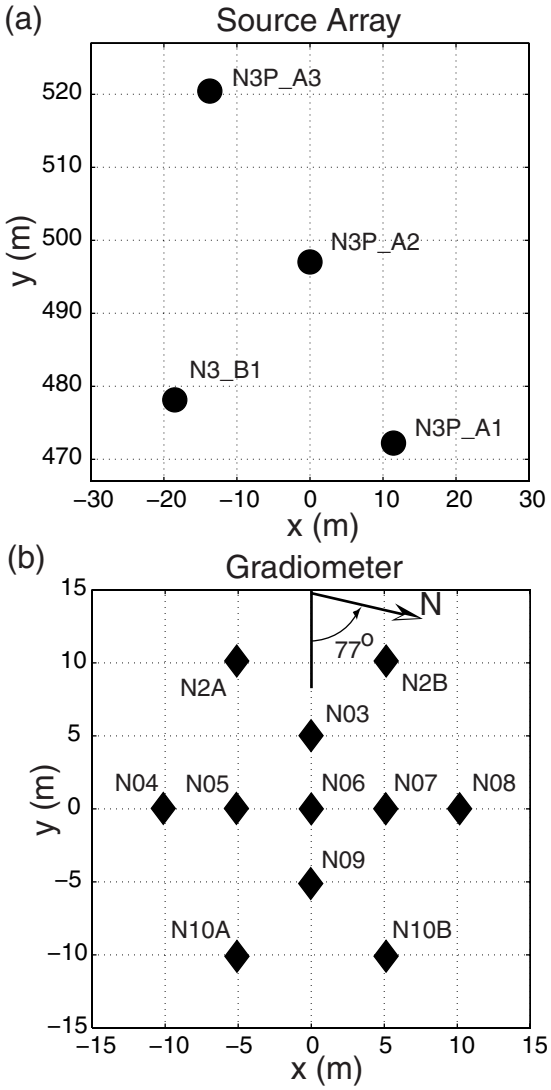

Figure 1. Geometry of (a) source and (b) gradiometer arrays from Lin *et al.* (2009). Boreholes for the N3P and N3 explosions are annotated in (a). Station names are annotated in (b). Note the direction of north relative to the *y* axis of the experiment coordinate system.

boreholes were placed in a Cartesian coordinate system with an origin at station N06 of the gradiometer and where the *y*-coordinate axis intersected the middle borehole of explosion N3P. Stations of the gradiometer were situated at the nodes of a 5 m grid. Lin *et al.* (2009) provide information on construction details and the exact locations of each station based on field survey measurements as well as detailed information on sensor calibration. Eight acceleration sensors were Metrozet TSA-100S sensors, and the others were Kinemetrics Episensor ES-T sensors. Quanterra Q330 data loggers were used to record the data at 200 samples/sec.

Theoretical Background

The basis for seismic-wave gradiometry is presented in Langston (2007a,b,c) and Langston and Liang (2008). In this

article, we perform gradiometry in two dimensions using the theory presented in Langston (2007b) and Langston and Liang (2008). In addition, the time domain method from Langston (2007c) is used to solve for the geometrical spreading and wave slowness coefficients in two dimensions. Because the technique is relatively new we review highlights as they pertain to the TAIGER explosion gradiometer.

The basic assumption in the technique is the nature of a propagating wave that contains geometrical spreading and wave slowness that might change with distance. For one dimension, say x, wave motion can be represented as

$$u(x, t) = G(x) f[t - p(x - x_0)], \tag{1}$$

where $G(x)$ is the distance-dependent geometrical spreading of the wave, p is the horizontal wave slowness (inverse horizontal phase velocity), and x_0 is a reference position. The spatial gradient of this wave is

$$u_{,x} = A_x u + B_x u_{,t}, \tag{2}$$

where the coefficients are

$$A_x = \frac{G'}{G}, \qquad B_x = -p - \frac{\partial p}{\partial x}(x - x_0). \tag{3}$$

The comma notation denotes the partial derivative with respect to space or time (e.g., $u_{,x} = \frac{\partial u}{\partial x}$) and the prime denotes the derivative with respect to the function argument. Equation (2) shows that there is a relationship between three different seismograms—the spatial gradient, the original wave field, and the time derivative of the original wave field. The coefficients of this relationship contain information on the change in geometrical spreading (A_x) and the wave slowness (B_x). The coefficients can be found if the three seismograms are available, so part of the analysis work involves measuring or determining the spatial gradient, $u_{,x}$. In principle, this can be done with strain meters and rotation meters (e.g., Langston and Liang, 2008) but is normally done by numerically differencing seismograms in a suitable array configuration. We use the inversion technique outlined in Langston and Liang (2008) that simultaneously uses all stations of the gradiometer shown in Figure 1. The wave field and its time derivative are readily available from a single array site.

The time domain method (Langston, 2007c) is used here to solve for the two coefficients once the spatial gradient has been determined. Equation (2) can be linearly transformed into its analytic signal form using the Hilbert transform to give

$$U_{,x} = A_x U + B_x U_{,t}, \tag{4}$$

where, for example,

$$U(t) = u(t) - iH[u(t)] \tag{5}$$

and

$$H[u(t)] = -\frac{1}{\pi t} * u(t). \tag{6}$$

Solving for the B_x coefficient gives

$$B_x = \frac{1}{\omega(t)} \frac{|U_{,x}|}{|U|} \sin(\psi - \phi), \tag{7}$$

where the absolute values of the analytic signals of the displacement gradient and displacement represent the instantaneous amplitude, or envelope functions, ψ and ϕ are the instantaneous phases of the displacement gradient and displacement, respectively, and $\omega(t)$ is the instantaneous frequency of the displacement. The A_x coefficient is

$$A_x = \frac{|U_{,x}|}{|U|} \cos(\psi - \phi) - \frac{1}{\omega(t)} \frac{|U_{,x}|}{|U|^2} \frac{\partial |U|}{\partial t} \sin(\psi - \phi). \tag{8}$$

There are isolated singularities in these solutions when there are zeros in the envelope function of the displacement. These are avoided in practice by only allowing amplitudes $|U| > 0.0005 \max |U|$.

A two-dimensional gradiometer problem consists of solving two one-dimensional problems in both x and y and relating results to coefficients for a propagating wave in cylindrical coordinates (Langston, 2007b; Langston and Liang, 2008). This wave has an addition attribute of radiation pattern where

$$u(t, r, \theta) = G_r(r) R(\theta) f[t - p_r(r - r_0)], \tag{9}$$

which gives an additional equation to solve

$$\frac{1}{r} \frac{\partial u}{\partial \theta} = \frac{\Re(\theta)}{r} u, \tag{10}$$

with solution

$$\frac{\Re(\theta)}{r} = \frac{1}{r} \frac{R'}{R} = A_x \cos\theta - A_y \sin\theta. \tag{11}$$

Wave azimuth is obtained by computing

$$\theta = \tan^{-1} \frac{B_x}{B_y}. \tag{12}$$

In summary, data from the gradiometer array are used to compute geodetic array spatial gradients from which strains and rotations can be obtained. The spatial gradients are then used to find the gradiometry coefficients A and B in Cartesian, then cylindrical coordinate systems. The coefficients in cylindrical coordinates are then plotted with the original data as a function of time to examine the original wave field, wave azimuth, wave slowness, the change in geometrical spreading, and the change in radiation pattern. All quantities are

used to interpret the seismogram in terms of wave type and how waves propagate.

Data Analysis

We chose to perform the gradiometry analysis using data over two frequency bands from 3 to 50 Hz, covering most of the bandwidth of the signal, and from 3 to 5 Hz, covering the low-frequency part of the signal, basically to separately examine the body wave and surface wave portions of the wave train. The instrument-corrected acceleration data were filtered with a 2-pole, causal Butterworth filter with the corners stated previously. The broadband data are dominated by high-frequency initial arrivals, presumably the *P*-wave train, over the first 0.5 sec (Fig. 2). The low-frequency bandpass data appear to be dominated by surface waves that have durations of several seconds (Fig. 3). We show processing results for both explosion sources on the order of the single-borehole explosion, N3, and then the triple-borehole explosion, N3P, expecting that source complexity or finiteness might be a factor for the N3P data.

The first step in gradiometry is to compute the vertical and horizontal displacement gradients using the finite difference inversion scheme. Figure 2 shows that the initial por-

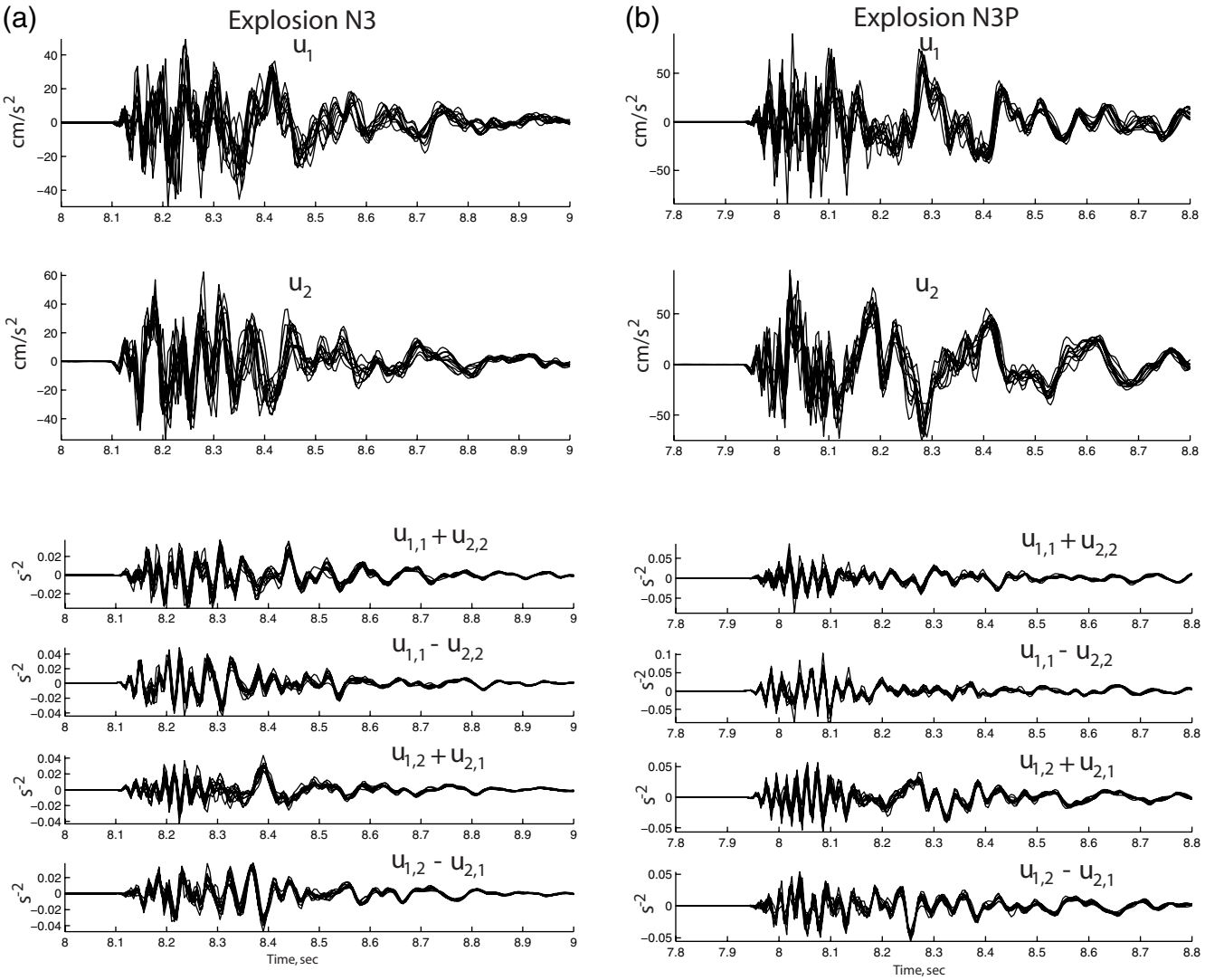

Figure 2. Broadband (3–50 Hz) horizontal component accelerations (u_1 and u_2) and resulting strains and horizontal rotations. Waveforms for the single-borehole explosion N3 are shown in (a) and those from the triple-borehole explosion N3P are shown in (b). u_1 and u_2 directions are for the x and y coordinate directions, respectively. The coordinate-invariant area strain is given by $u_{1,1} + u_{2,2}$. The differential normal strain is $u_{1,1} - u_{2,2}$. $u_{1,2} + u_{2,1}$ is twice the shear strain in the x–y coordinate system, and $u_{1,2} - u_{2,1}$ is the negative of twice the horizontal rotation about the vertical axis. Because we are dealing in filtered acceleration, not displacement, the units for strain and rotation are in sec^{-2}. Note that the filtered accelerations, strains, and horizontal rotation are shown for all sensor positions. In particular, each sensor was chosen as the reference sensor position to calculate strain and rotation in the inverse method (see Langston and Liang, 2008). Superimposing all waveforms gives a sense for the variance in the data and the computations. The reference times between events N3 and N3P shown in the plots are arbitrary.

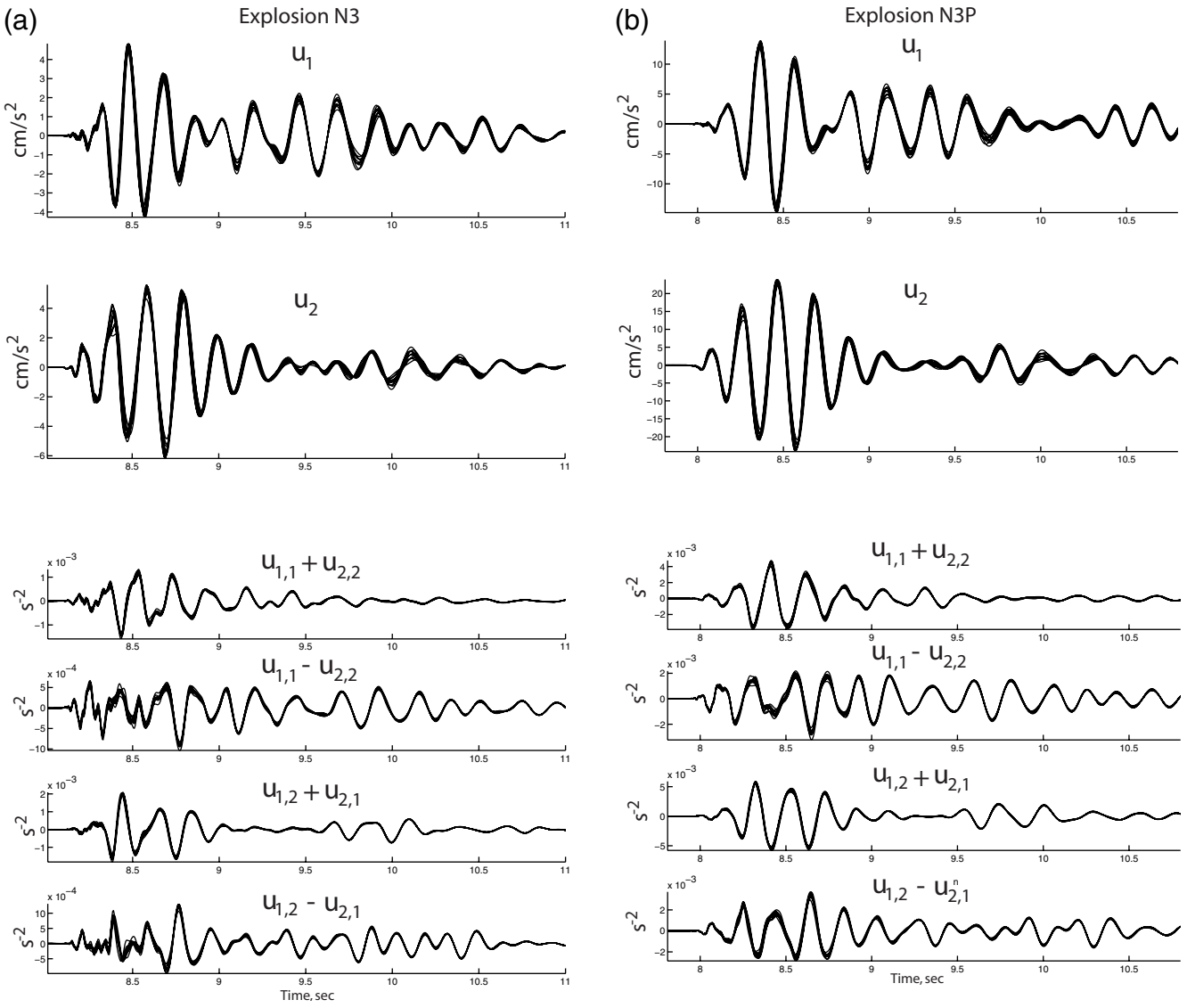

Figure 3. Low-frequency pass band (3–5 Hz) horizontal component data for explosion (a) N3 and (b) N3P. Same scheme as in Figure 2.

tions of the broadband horizontal data are dominated by ~40 Hz waves that can change by a factor of 2 in amplitude across the gradiometer. The portion of the strain and rotation tensor that can be obtained from gradients of the horizontal accelerations (Fig. 2) show that these amplitude variations are not too detrimental to the strain and rotation calculation because there is considerable averaging through use of all 11 elements of the gradiometer. Even so, some peaks and troughs in the strain and rotation show 100% variances in amplitude but that the phases of all signals are generally consistent. The initial portion of data from N3P also appears to be higher in frequency content than from the same time interval for N3 and displays greater waveform variance. However, the strains and rotation appear to display less variance for N3P data compared to N3, which seems surprising. The low-pass band data (Fig. 3) show much less variance for both explosions with excellent strain and rotation estimates.

The first observation that can be made from the strains and rotation is that the data are inconsistent with an axisymmetric explosion source model. Although the seismic gradiometer is only about 500 m from the explosion sources, this distance is still several seismic wavelengths from the source point. For example, a 40 Hz *P* wave with a horizontal phase velocity of 4000 m/sec and a 6 Hz Rayleigh wave traveling at 1800 m/sec have horizontal seismic wavelengths of 100 and 300 m, respectively. Ground motion for an axisymmetric source will ideally be confined to the radial-vertical plane with no azimuthal radiation pattern and no transverse component motions. The area strain and differential strain for a source located on the *y* axis of the gradiometer in an ideal vertically inhomogeneous Earth model will differ only by sign (waveforms will be identical), and the shear strain and horizontal rotation will be zero. The broadband data of Figure 2 show that horizontal rotation is comparable to the area

strain. The area strain is a coordinate system invariant, as is the horizontal rotation, and both indicate the relative levels of *P-SH* and *SH* motions, respectively (Langston and Liang, 2008). The relative amounts of area strain and horizontal rotation are also comparable for the low-frequency band-pass data (Fig. 3). Thus, these data suggest that each source was not axisymmetric such that they each radiated significant *SH* and Love waves, or that the propagation medium is heterogeneous, coupling waves onto all components, or both. Strains and rotation show that the wave propagation is more complex than could be inferred from the particle motions alone.

Figures 4 and 5 show the results of a time domain gradiometry analysis on the filtered vertical component data as outlined by equations (1)–(12). In these figures, major arrivals are highlighted across the wave parameter plots of azimuth, horizontal slowness, the geometric spreading change, and radiation pattern change. Table 1 lists means and standard deviations of all wave parameters estimated within the individual time windows. The initial 0.1 sec of the vertical

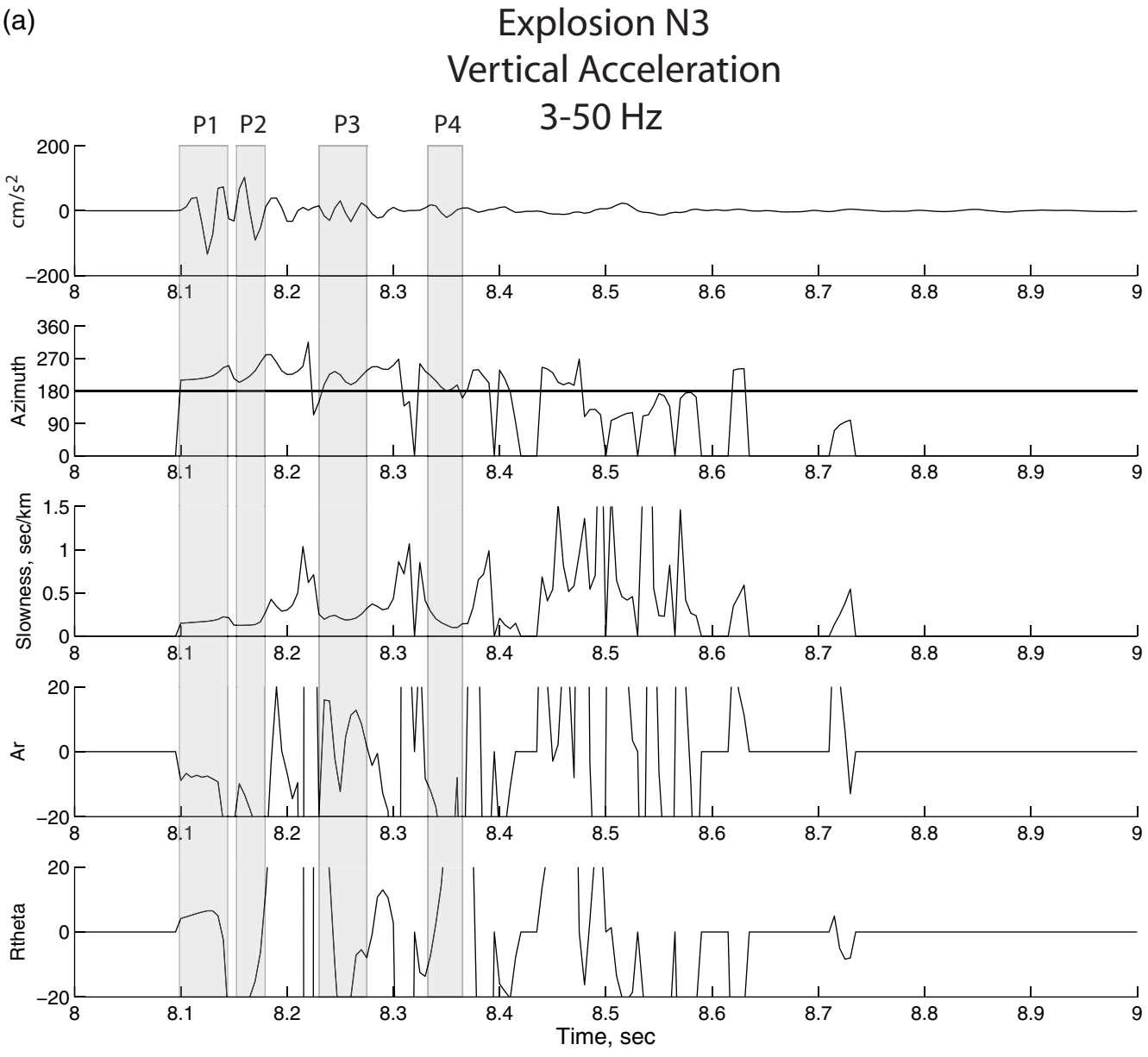

Figure 4. Vertical component, broadband (3–50 Hz) gradiometry result for explosion (a) N3 and (b) N3P. The upper panel shows 1 sec of filtered acceleration data, in this case, the *P* waveform. The panel titled "Azimuth" shows the estimated azimuth of wave propagation (direction that the wave is moving) measured clockwise relative to the *y* axis direction of the coordinate system. The dark line at 180° azimuth is the expected straight-line path azimuth for all waves from the explosions. The shaded boxes highlight portions of the data and wave attribute graphs. The estimated wave slowness in sec/km is given in the middle panel with the change in radial geometrical spreading (panel titled "Ar") and change in radiation pattern (panel titled "Rtheta") given in the lower two panels. (*Continued*)

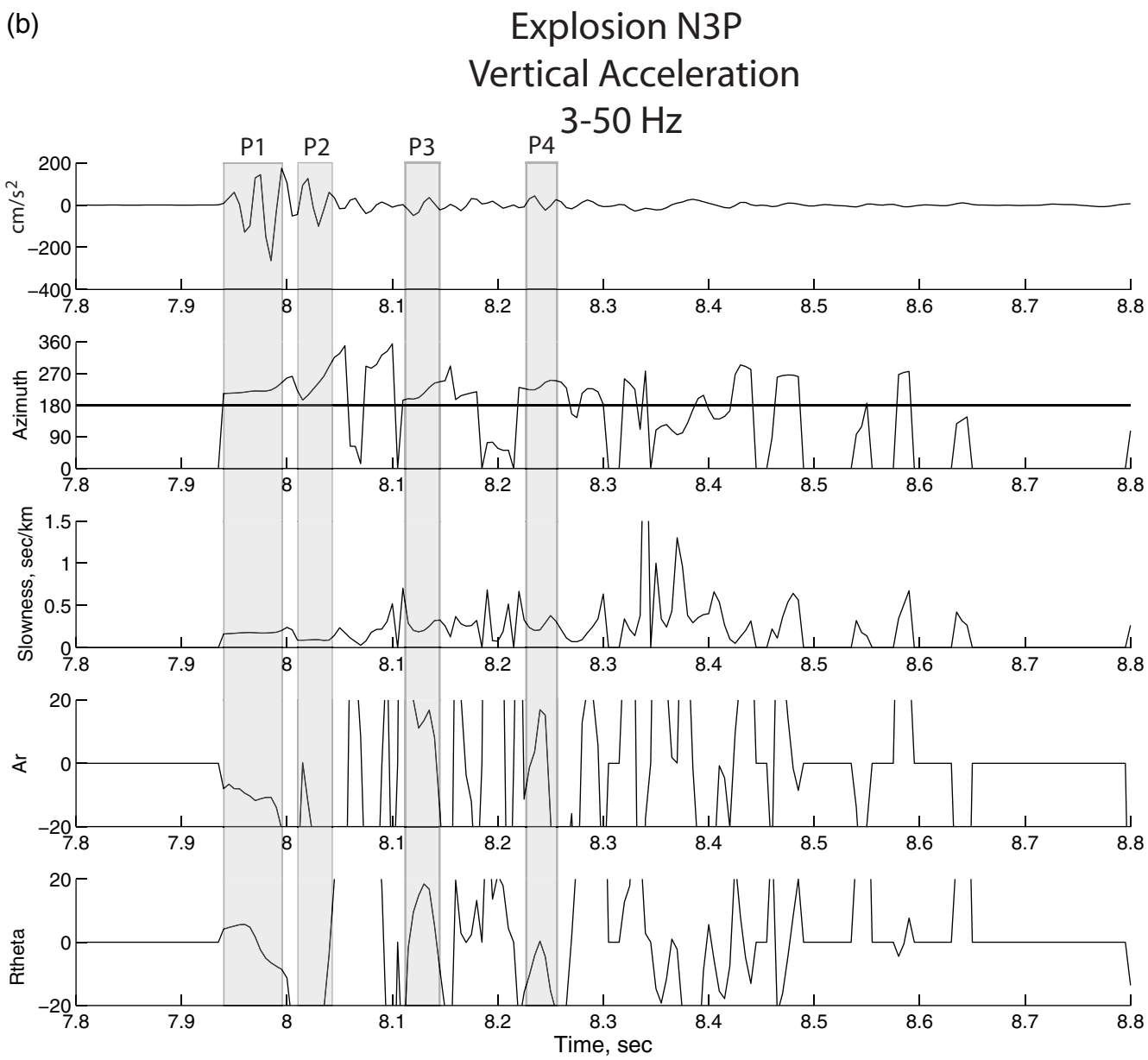

Figure 4. Continued.

component (Fig. 4) is roughly ten times larger than the corresponding time interval on the horizontal components suggesting the standard seismological interpretation that this is the *P*-wave arrival and that it must have a relatively small angle of incidence. The gradiometry result shows that this phase has a horizontal velocity of ~5800 m/sec, consistent with the particle motion observation but that it is traveling in a direction about 215° clockwise from the *y* axis. This is 35° off-azimuth from the expected theoretical radial direction. The variation in source position from the *y* axis based on field borehole positions can only give about 2° difference in azimuth. Both slowness and azimuth are seen to change slowly with time, and there is also a correlation of large changes in the geometrical spreading change and radiation pattern with the last half of the arrival (P2 in Fig. 4) in the time window. This suggests that more than one phase may be arriving in the initial 0.1 sec. Later phases also have relatively low slowness (high velocity), and all *P* waves have similar azimuth anomalies (Fig. 4).

The character of the gradiometry plots is dominated by two effects. The first is concerned with the amplitude threshold used in computing the coefficients mentioned previously. For these times on the records, all of the parameters are set to zero, causing pronounced discontinuities and flat spots. The other effect is intrinsic to the time domain method. The interference of two or more phases can cause discontinuities in the instantaneous frequency and time derivative of envelope functions (Langston, 2007c). These appear as spikes. It

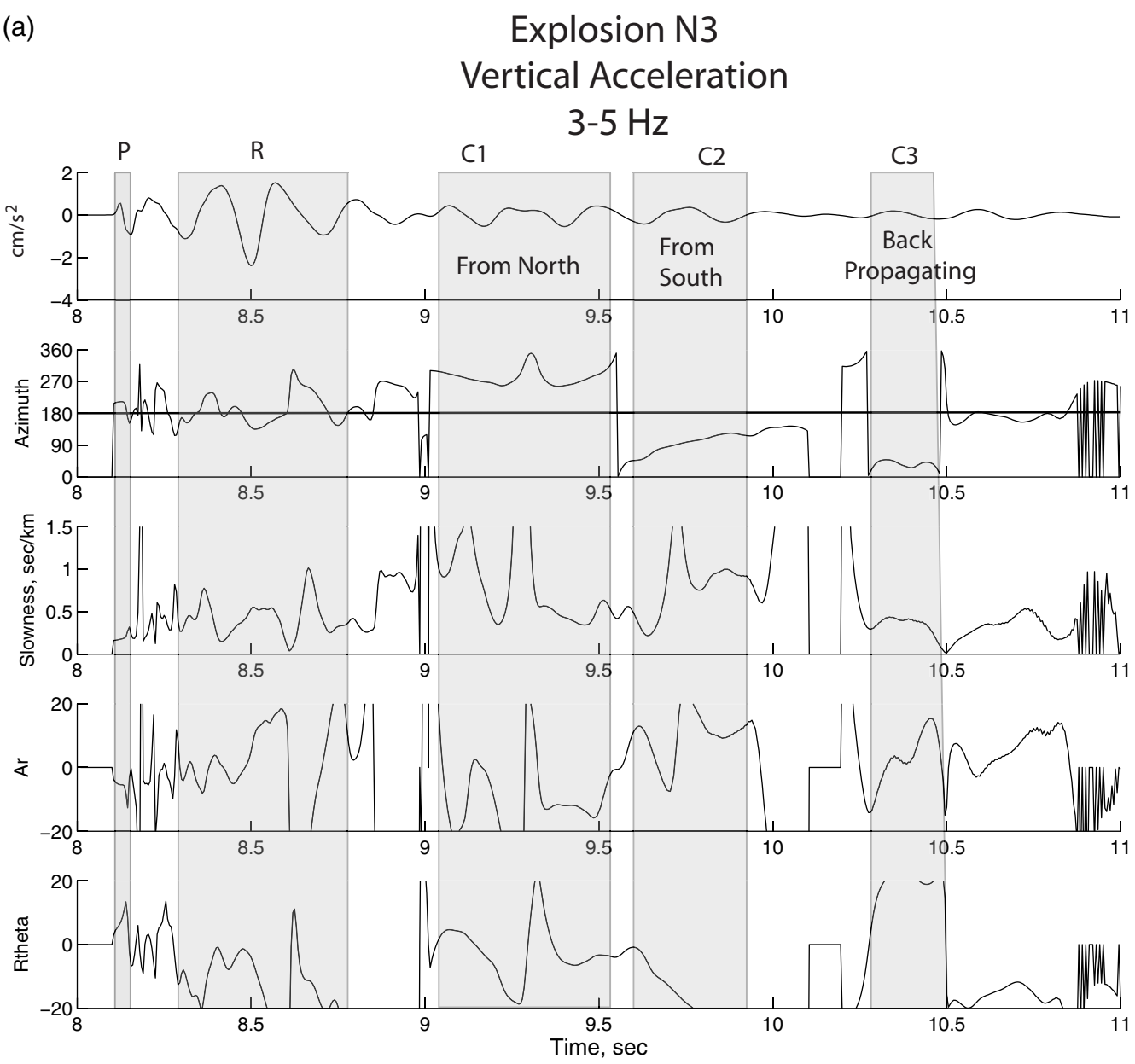

Figure 5. Vertical component, low-frequency pass band gradiometry result for explosion (a) N3 and (b) N3P. Same scheme as in Figure 4. The earliest arrival highlighted is the *P* wave. Later arrivals in this pass band are low-velocity surface waves that propagate in all directions indicating velocity and topographic heterogeneity. (*Continued*)

is helpful to time window around specific high-amplitude phases to examine wave characteristics. Spikes and other artifacts usually occur where signal levels are small.

At lower frequency (Fig. 5), gradiometry gives the same result for the initial *P*-wave part of the record as seen in Figure 4 but with higher variance (Table 1). The major arrival starting about 0.25 sec after the *P*-wave arrivals could be an ~6 Hz Rayleigh wave with a phase velocity as high as 3 km/sec. Azimuth seems to change throughout this waveform for explosion N3 but is relatively stable at 180° for explosion N3P. Other coda waves, for both explosions, show that very low-velocity (high slowness) waves propagate north and south across the river valley and even back towards the source. This is a fascinating observation of wave scattering obtained essentially by a point measurement.

The Rayleigh wave was investigated using horizontal component gradiometry (Fig. 6). Horizontal component particle motions for the Rayleigh-wave phase are four to five times larger than vertical motions. The horizontal component Rayleigh wave also displayed higher precision in the azimuth estimate compared to the vertical Rayleigh wave (Table 1). Figure 6 shows one analysis where the horizontal x and y motions were vectorially rotated so that an azimuth of 135° from the y axis would be the radial particle motion direction

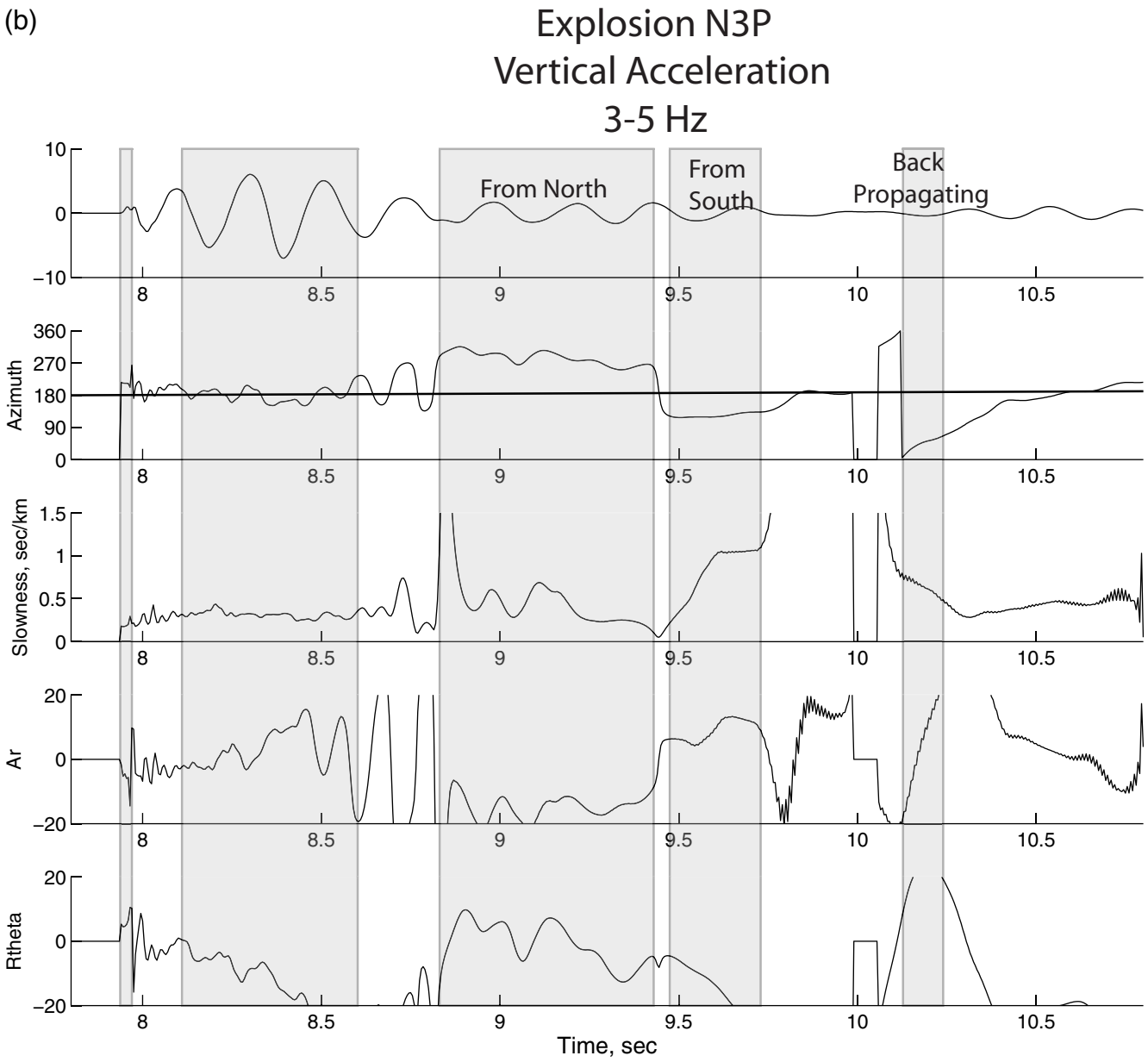

Figure 5. Continued.

consistent with the inferred wave propagation direction. It should be noted that most any rotation of the horizontal component data yields the same direction of wave propagation because it is the gradiometer array element positions that control the estimation of azimuth through the finite difference computation (Langston and Liang, 2008).

Figure 6 shows that the initial Rayleigh wave propagates in a 135° azimuth with little change across its waveform, unlike the variations seen in the vertical data (Fig. 5). The slowness changes from 0.5 to 0.75 sec/km across the time window suggesting dispersion from 2 to 1.3 km/sec in phase velocity. The geometrical spreading change is slightly negative, consistent with a propagating wave that decreases in amplitude with distance, although these estimates have high variance (Table 1). The horizontal component gradiometry also shows similar azimuth behavior for later arriving coda waves as seen in the vertical component data.

Discussion

Figure 7 shows a Google map image of the experiment area. The experiment occurred in the Zhu-shiu river valley within a rugged mountainous region of Taiwan that can have about 1000 m of elevation change in a few kilometers. The material making up the river sediment is quite heterogeneous as shown in Lin *et al.* (2009). However, it is likely that the

Table 1
Wave Parameter Estimates*

Phase	Azimuth (°)	Slowness (sec/km)	Geometrical Spreading Change	Radiation Pattern Change
Explosion N3, 3–50 Hz (Fig. 4a)				
P1	217 (7)	0.170 (0.014)	−8 (1)	6 (1)
P2	218 (14)	0.129 (0.004)	−16 (6)	−26 (11)
P3	207 (25)	0.220 (0.027)	4 (13)	0 (32)
P4	192 (20)	0.161 (0.066)	−30 (21)	51 (54)
Explosion N3P, 3–50 Hz (Fig. 4b)				
P1	219 (5)	0.173 (0.005)	−10 (2)	1 (5)
P2	235 (33)	0.088 (0.003)	−30 (19)	−38 (24)
P3	211 (19)	0.310 (0.181)	42 (66)	3 (20)
P4	234 (12)	0.274 (0.071)	1 (14)	−8 (7)
Explosion N3, 3–5 Hz (Fig 5a)				
P	193 (24)	0.210 (0.060)	−5 (3)	4 (7)
R	196 (43)	0.417 (0.180)	−2 (18)	−19 (17)
C1	279 (37)	0.8 (0.8)	−13 (15)	−2 (8)
C2	115 (12)	1.1 (0.3)	10 (8)	−27 (7)
C3	55 (10)	0.33 (0.08)	12 (6)	18 (5)
Explosion N3P, 3–5 Hz (Fig. 5b)				
P	212 (24)	0.202 (0.038)	−3 (8)	3 (8)
R	183 (21)	0.314 (0.040)	2 (8)	−15 (10)
C1	283 (18)	0.5 (0.4)	−15 (4)	−1 (7)
C2	126 (7)	1.00 (0.34)	8 (6)	−19 (9)
C3	62 (15)	0.52 (0.12)	18 (11)	19 (6)
Explosion N3 Radial Component, 3–5 Hz (Fig. 6a)				
R	135 (6)	0.65 (0.15)	−3 (3)	2 (1)
C1	244 (24)	0.8 (0.3)	9 (7)	14 (17)
C2	85 (20)	0.78 (0.19)	11 (1)	−19 (8)
C3	39 (5)	0.96 (0.27)	6 (17)	17 (4)
Explosion N3P Radial Component, 3–5 Hz (Fig. 6b)				
R	132 (2)	0.66 (0.11)	−2 (2)	1 (2)
C1	271 (36)	0.83 (0.32)	−1 (7)	7 (13)
C2	150 (19)	1.00 (0.19)	6 (5)	−36 (8)
C3	21 (6)	0.96 (0.15)	−3 (13)	25 (8)

*Standard deviation is given in parentheses.

hillsides have higher seismic velocities than river fill sediments. The depth configuration of the river channel is not known nor are near-surface velocity measurements available of channel fill or hill slope materials. Nevertheless, at the seismic wavelengths considered here of 100–300 m, the experiment area has significant topographic and velocity heterogeneity that can be appealed to for the observations of wave scattering seen in the gradiometry analysis.

Few waves are actually seen to propagate straight from the source to the gradiometer. The observed *P* wave from each explosion travels at high-apparent velocity characteristic of high-velocity basement rocks and arrives 35° off-azimuth. One hypothesis consistent with this observation is that the base of the river channel dips to the south producing the off-azimuth refraction. The initial Rayleigh wave arrives 45° off-azimuth from the south side of the valley. Perhaps it is a reflection from the steep topographic river-cut there or, maybe, a product of horizontal refraction due to horizontal velocity variations in river fill. In any of these cases, data about the nature of the wave propagation have been obtained that can be used to build hypotheses and better experiments to test those hypotheses. It would be difficult to infer any of these wave characteristics from a single accelerometer.

Although the aperture of the gradiometer was well within 10% of the seismic wavelengths analyzed here, we nevertheless attempted to use standard frequency–wavenumber methods to check the azimuth and slowness estimates obtained from wave gradiometry. Applying broadband frequency–wavenumber methods (Nawab *et al.*, 1985) on the vertical component data in the 40–50 Hz band yielded a wave propagation azimuth of 242° and a horizontal phase velocity of 5.2 km/sec for the peak power, close to the gradiometry result for propagating *P* waves. Analyzing the 5–7 Hz band pass yielded an azimuth of 137° and a horizontal wave speed of 2.0 km/sec, similar to the Rayleigh-wave result. However, these estimates have very large variances considering that the area encompassed by half the peak power in the frequency–wavenumber spectrum encompasses all azi-

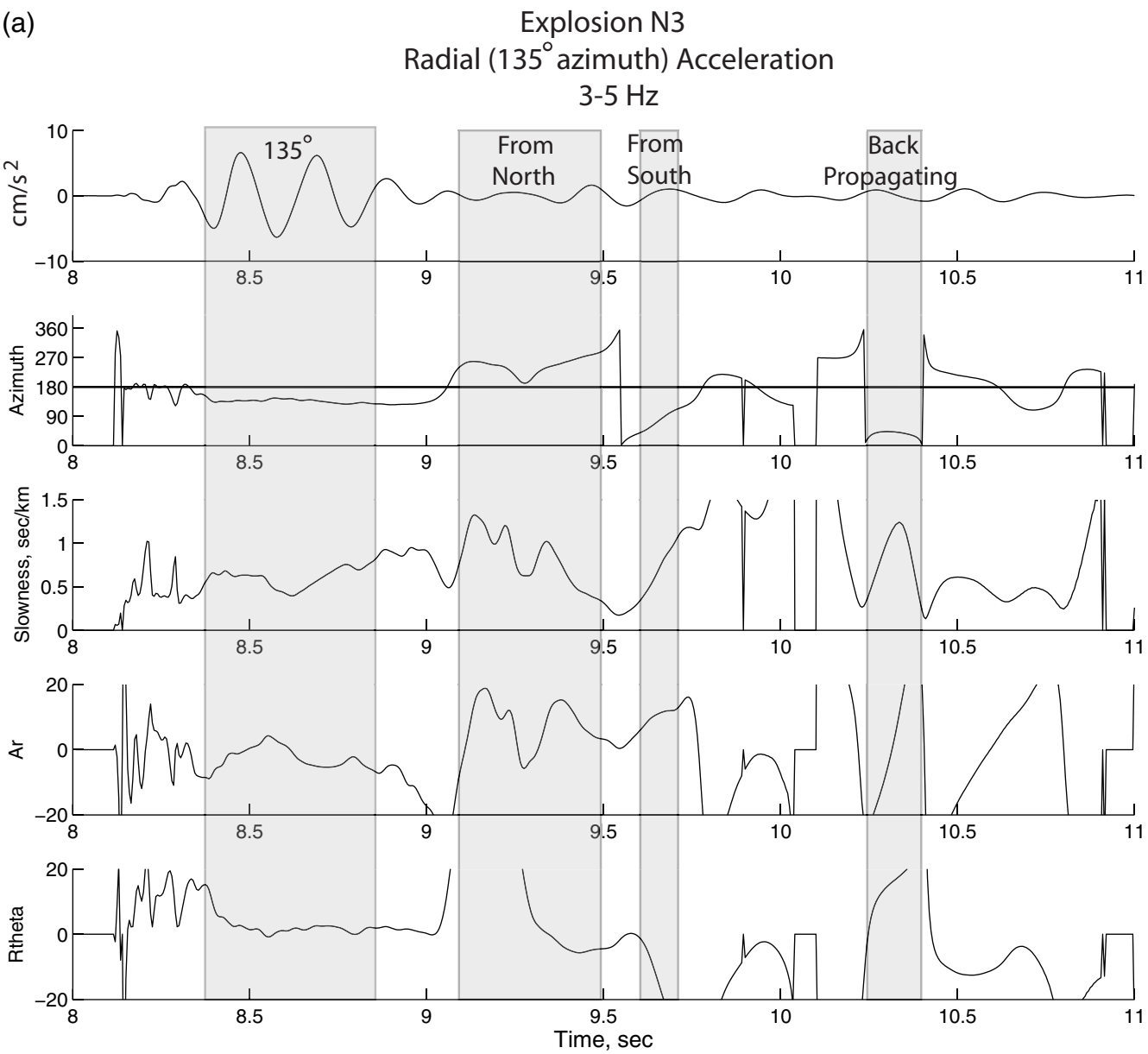

Figure 6. Horizontal component, low-frequency pass band gradiometry result for explosion (a) N3 and (b) N3P. Same scheme as in Figure 4. The horizontal data have been vectorially rotated into the direction of 135° within the Cartesian coordinate system of the experiment. The azimuth estimate for the large, initial Rayleigh wave remains at 135° over the duration of the phase, consistent with the inferred particle motion. (*Continued*)

muths and horizontal velocities as low as 1 km/sec and as high as infinity for both waves. It is probably fortuitous that the estimates agree so well.

Gradiometry is based on the assumption of a single propagating wave but has been successfully used in previous studies to analyze seismograms with many interfering waves for one and two dimensions (Langston, 2007a,b,c; Langston and Liang, 2008). Figure 8 shows a gradiometry result for a synthetic seismogram computation assuming a layer-over-half-space Earth model, an isotropic point source, and a gradiometer array in the same configuration as used in our experiment (Fig. 1). As with other synthetic seismogram experiments (e.g., Langston and Liang, 2008), gradiometry yields expected wave parameters for various phases in the synthetic wave trains. Azimuth can be found within 0.5° and wave slownesses for individual seismic phases to within a few percent. However, the interference of waves throughout the seismogram causes artifacts that progressively get larger in the order of azimuth, slowness, geometrical spreading change, and radiation pattern change. This behavior is reproduced in the analysis of the field data (Figs. 4–6 and Table 1) where wave direction azimuths and slownesses generally have smaller relative variances than geometrical spreading and radiation pattern changes. The best parameter

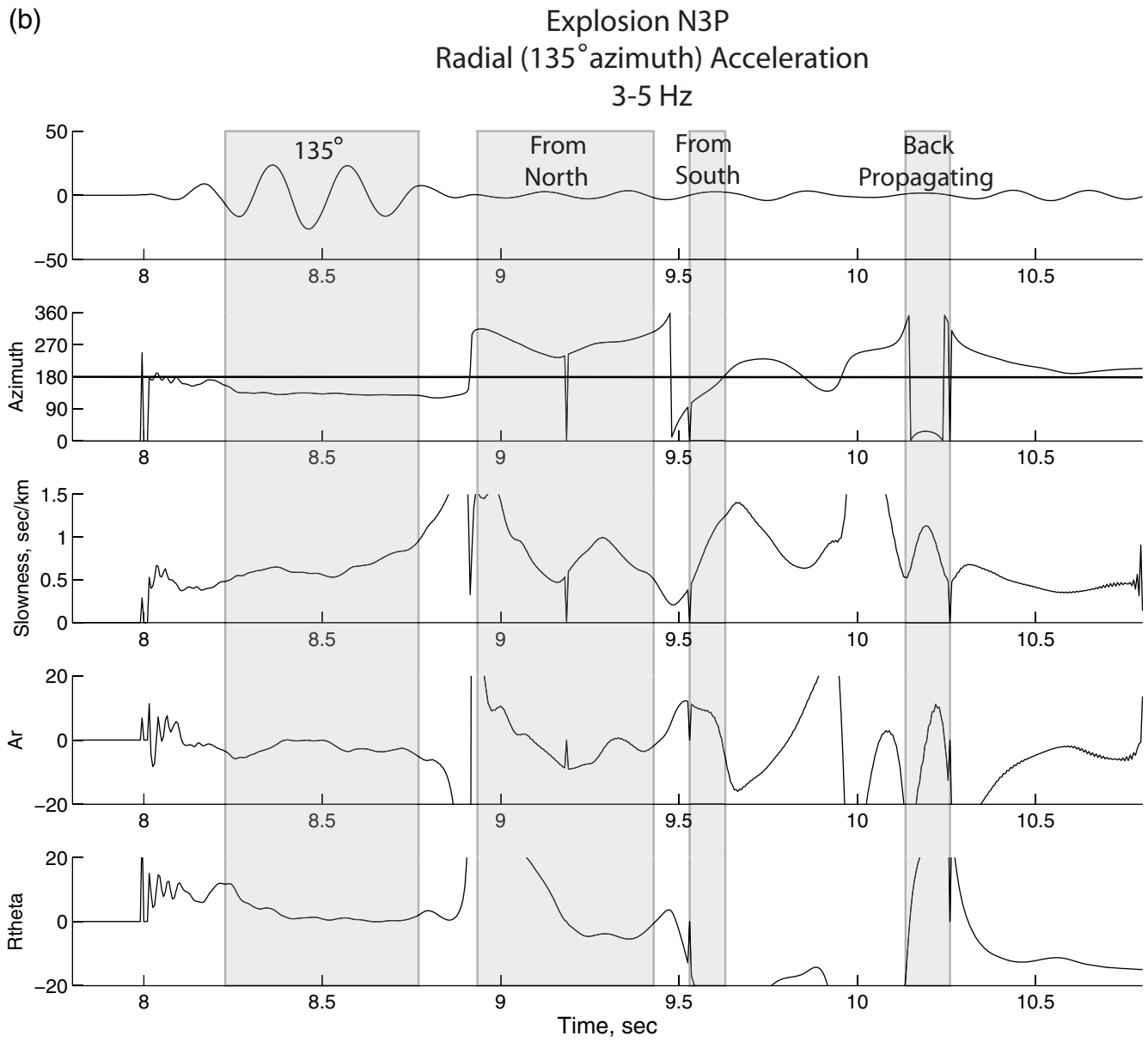

Figure 6. Continued.

estimates seem to always occur, theoretically, at the peak-wave amplitude. The character of the synthetic results in Figure 8 is similar to that seen in the broadband data of Figure 4. The interference of the synthetic refracted *P*, reflected *P*, and direct *P* waves show increasing slowness with time, and there are large changes in the geometrical spreading parameter when the waves interfere.

The high-frequency strains and rotation (Fig. 2) show significant variability that probably reflects velocity heterogeneity directly under the gradiometer site or instrumentation site response differences at higher frequencies. We computed the strains, rotations, and high-frequency gradiometry analyses using only the inner five stations of the gradiometer. This is an ideal, second-order accuracy finite difference star geometry with the closest available station spacing. The effects of velocity heterogeneity should be at a minimum. However, the broadband data has as much variability for the small, dense array as it does for the entire 11-element array. Even so, gradiometry results for the smaller array were identical to that of the entire array, so we show results from the entire array for completeness.

Although explosion N3P used four times more explosives than N3, it is surprising to see that high-frequency signal levels are only about 100% larger for N3P compared to N3 (Fig. 2). This was noted by Lin *et al.* (2009). However, the waves in the long-period pass band have an amplitude ratio very close to four; this suggests that there is a significant effect of source radiation pattern for explosion N3P at higher

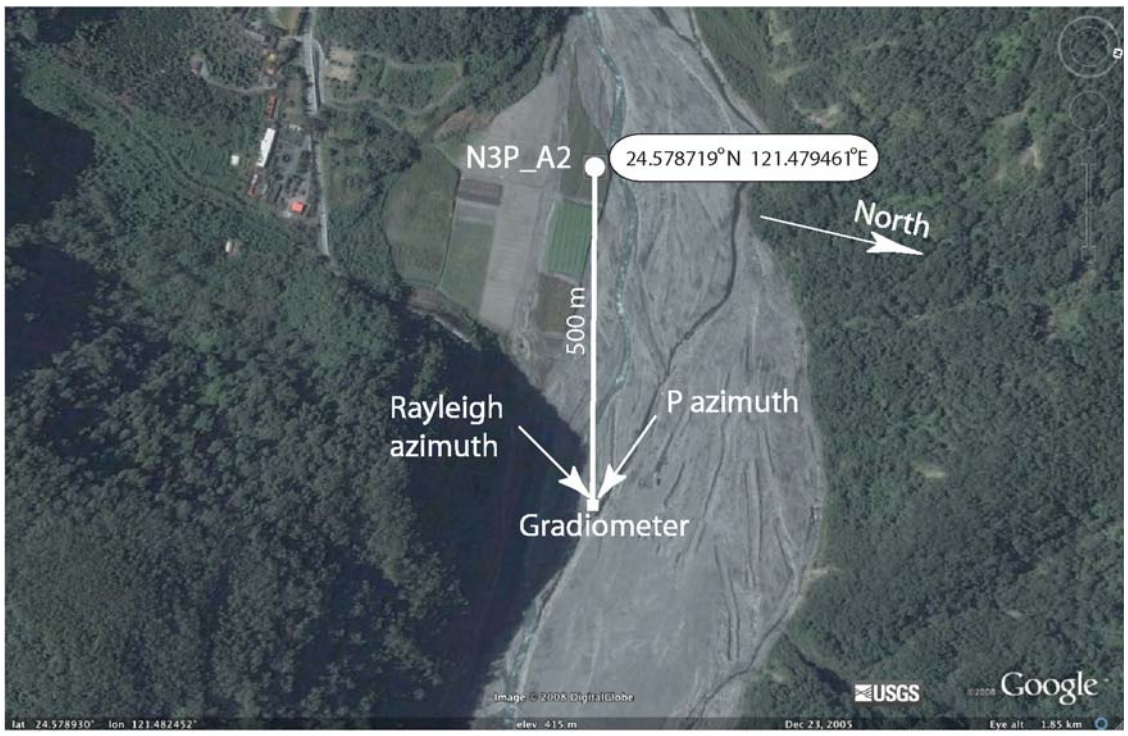

Figure 7. Google map image of the experiment environment. The region just to the left of the gradiometer position is in shadow. Gravel of the river valley are gray-colored, and farm fields can be seen in the area of borehole N3P_A2. The distance between N3P_A2 and element N06 of the gradiometer is 496 m. Rayleigh- and *P*-wave azimuths of propagation are shown by the arrows.

frequencies. The horizontal radiation pattern due to the interference of three axisymmetric sources can be estimated with a simple calculation. Assuming equal sized borehole sources, the displacement, $u(t)$, for a particular seismic wave is given by

$$u(t) = S(t - pr_1) + S(t - pr_2) + S(t - pr_3), \qquad (13)$$

where r_i is the distance from the source point to a receiver and p the wave horizontal slowness (inverse horizontal phase velocity) of the seismic wave under consideration. Note, that we are assuming that the Green's function does not appreciably change for the particular wave from each source if the sources are close together relative to the receiver position. Fourier transforming this equation and factoring out the phase of the reference center borehole (borehole number 2) gives

$$\hat{u}(\omega) = \hat{S}(\omega)e^{-i\omega pr_2}R(\theta, \omega, p), \qquad (14)$$

where the source radiation pattern is defined as

$$R(\theta, \omega, p) = 1 + e^{-i\omega p(r_1 - r_2)} + e^{-i\omega p(r_3 - r_2)}, \qquad (15)$$

and

$$x = r_2 \sin\theta, \qquad y = r_2 \cos\theta. \qquad (16)$$

Figure 9 shows the amplitude spectrum value for the source radiation pattern (equation 15) assuming the source geometry of explosion N3P (Fig. 1), a radius $r_2 = 500$ m from the central borehole, a horizontal slowness of 0.2 sec/km (5 km/sec), and a frequency of 40 Hz, appropriate for the first arriving *P* wave. A 40 Hz *P* wave radiated at an azimuth of 180° would have about 60% of the amplitude at the radiation maximum of three. The amplitude could be 50% if radiated with an azimuth anomaly of 35° (azimuth of 145°) that might be consistent with the dipping refractor hypothesis. In any case, the geometry of explosion N3P relative to the gradiometer array suggests that *P* motion should only be about twice the motion of explosion N3. The value obtained from the vertical broadband data of Figure 4 is two, consistent with the radiation pattern hypothesis. At lower frequency, the effect of the radiation pattern becomes much less and is not important at all for 6 Hz Rayleigh waves, again consistent with the data. Although there is considerable evidence for wave scattering effects in the Zhu-shui river valley, simple source kinematics can explain the general amplitude features of the strong-motion data.

Conclusions

The use of seismic-wave strains, rotations, and displacement gradients in addition to standard vector particle motion observations is a way to more directly view seismic-wave propagation at a point in the Earth. A standard seismogram

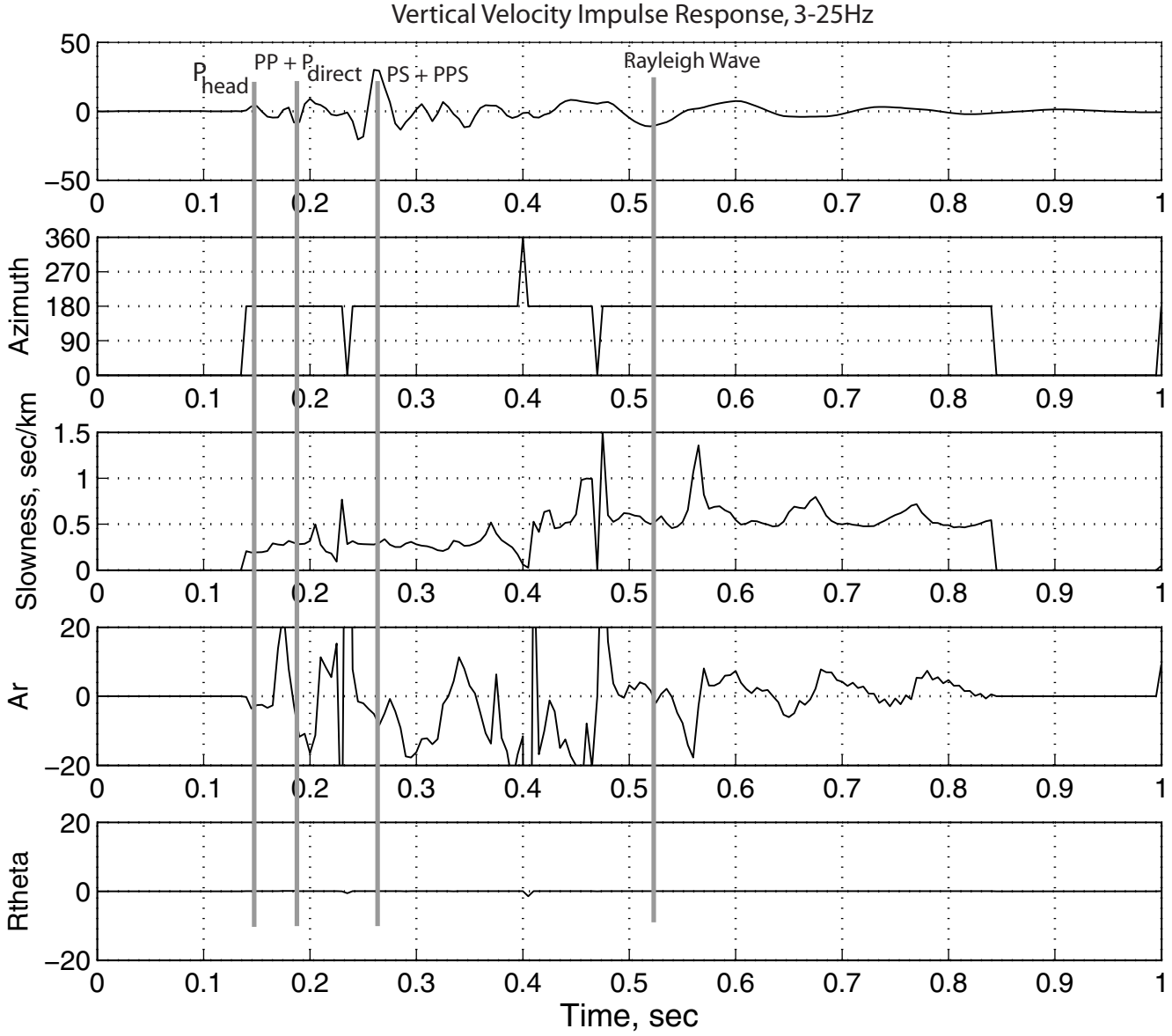

Figure 8. Vertical component gradiometry result for full-wave synthetic seismograms computed for a layer- ($V_P = 2.8$ km/sec, $V_S = 1.4$ km/sec, density $= 2.0$ g/cc, thickness $= 100$ m, $Q_P = 200$, $Q_S = 100$) over-half-space ($V_P = 5.0$ km/sec, $V_S = 2.87$ km/sec, density $= 2.7$ g/cc, thickness $= 100$ m, $Q_P = 500$, $Q_S = 250$) model. An isotropic point source is placed at 50 m depth in the layer. Amplitude is arbitrary but ground motion is velocity for a step in seismic moment and the synthetic data have been filtered between 3 and 25 Hz so that important *P* and Rayleigh phases can be seen. The gradiometry plots are similar in scheme to Figure 4. The source origin is exactly 500 m from station N06 using the same gradiometer geometry as shown in Figure 1b. Azimuth for all waves is 180°, and there is no radiation pattern for this axisymmetric source. Important phases are annotated.

represents only the amplitude of wave motion at a point. Wave spatial gradients yield strain and rotation that are a closer reflection of the physical state of the propagation medium and the nature of the seismic wave (e.g., Spudich *et al.*, 1995; Langston, 2007a). When combined with the original wave motion, wave spatial gradients can yield useful properties of seismic waves including propagation direction, speed, geometrical spreading changes, and radiation pattern changes. The simplicity or complexity of the seismogram can be viewed directly through a gradiometric analysis of the wave field.

These notions were tested using a specially designed seismic array, or gradiometer, consisting of 11 strong-motion, highly calibrated accelerographs situated at about 500 m from two large explosion sources in Taiwan. The aperture of the gradiometer was only 20 m and was used to analyze the local wave field in acceleration in the frequency band of 3–50 Hz. The horizontal strains and rotation derived from the accelerations using a finite difference inversion method showed that the wave propagation was not consistent with axisymmetric explosion sources. The area strain, representing *P-SH*-wave motion, and horizontal rotation, repre-

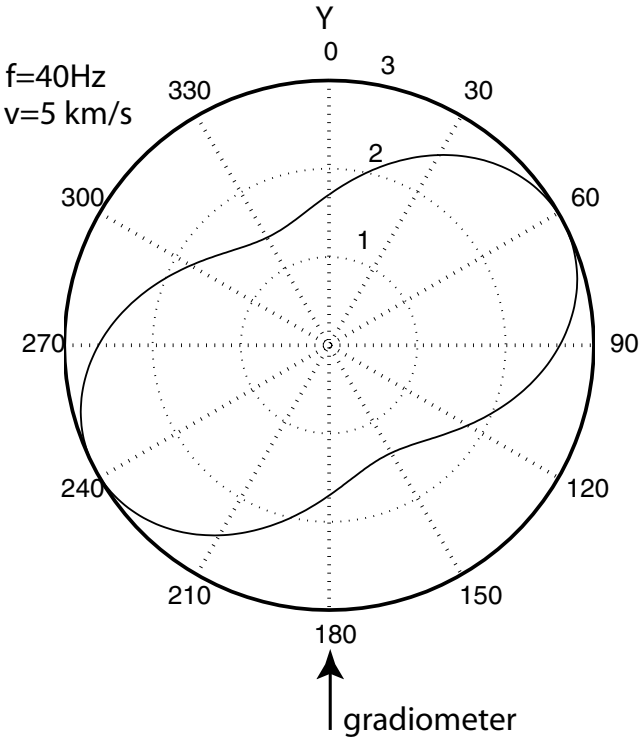

Figure 9. Polar plot showing the expected radiation pattern amplitude for the triple-borehole explosion N3P (using equation 15) for a 40 Hz *P* wave with a horizontal phase velocity of 5 km/sec. The azimuth to the gradiometer is shown by the arrow.

senting *SH*-wave motion, were of equal magnitude over the frequency band and suggested that the sources may have radiated Love waves or that the propagation medium is heterogeneous, or both. Gradiometry analysis of the three-component data showed that the *P* wave arrived 35° off-azimuth, in a clockwise direction, but that the Rayleigh wave arrived 45° off-azimuth in a counterclockwise direction. Low-frequency, slowly propagating surface waves later in the coda propagate back and forth across the river valley and even back toward the source, consistent with wave propagation in an area with large topographic and lateral velocity heterogeneity. Even so, frequency-dependent wave amplitudes between sources could be explained with a simple analysis of radiation pattern from the larger, triple-borehole explosion source.

We conclude that gradiometry does reveal a wealth of information on the composition of the wave field from these explosion sources and the nature of wave propagation in a heterogeneous medium. As seen in the variance estimates, wave parameter determinations generally degraded in the order of azimuth, slowness, geometrical spreading change, and radiation pattern change. The geometric design of the gradiometer and redundancy of instrumentation made it possible to usefully apply these techniques, even with the observation of short wavelength variations in acceleration across the array.

Data and Resources

All translational seismograms described in this article were collected by Lin *et al.* (2009). The data will be archived at the web site of the International Working Group on Rotational Seismology (http://www.rotational-seismology.org/) for open access. Seismic analysis code (Goldstein *et al.*, 2003) was used in part of the data processing and is gratefully acknowledged.

Acknowledgments

Part of this research was supported by the National Science Foundation under Grant Number EAR-0745898. We thank Marco Stupazzini and an anonymous reviewer for comments that improved the manuscript.

References

Aki, K., and P. G. Richards (1980). *Quantitative Seismology—Theory and Methods* W. H. Freeman and Co., San Francisco, California.

Goldstein, P., D. Dodge, M. Firpo, and L. Minner (2003). SAC2000: signal processing and analysis tools for seismologists and engineers, in *IASPEI International Handbook of Earthquake and Engineering Seismology, Part B* W. H. K. Lee, H. Kanamori, P. C. Jennings, and C. Kisslinger (Editors), Academic, New York, 1613–1614.

Havskov, J., and G. Alguacil (2004). *Instrumentation in Earthquake Seismology,* Springer, Dordrecht, The Netherlands.

Langston, C. A. (2007a). Spatial gradient analysis for linear seismic arrays, *Bull. Seismol. Soc. Am.* **97,** 265–280.

Langston, C. A. (2007b). Wave gradiometry in two dimensions, *Bull. Seismol. Soc. Am.* **97,** 401–416.

Langston, C. A. (2007c). Wave Gradiometry in the time domain, *Bull. Seismol. Soc. Am.* **97,** 926–933.

Langston, C. A., and C. Liang (2008). Gradiometry for polarized seismic waves, *J. Geophys. Res.* **113,** B08305, doi 10.1029/2007JB005486.

Lin, C.-J., C.-C. Liu, and W. H. K. Lee (2009). Recording rotational and translational ground motions of two TAIGER explosions in northeastern Taiwan on 4 March 2008, *Bull. Seismol. Soc. Am.* **99,** no. 2B, 1237–1250.

Nawab, S., F. Dowla, and R. Lacoss (1985). Direction determination of wideband signals, *IEEE Trans. Acoust. Speech, Signal Process.* **33,** 1114–1122.

Spudich, P., L. K. Steck, M. Hellweg, J. B. Fletcher, and L. M. Baker (1995). Transient stresses at Parkfield, California, produced by the *M* 7.4 Landers earthquake of June 28, 1992: observations from the UPSAR dense seismograph array, *J. Geophys. Res.* **100,** 675–690.

Center for Earthquake Research and Information
University of Memphis
3876 Central Avenue, Suite 1
Memphis, Tennessee 38152-3050
(C.A.L.)

862 Richardson Court
Palo Alto, California 94303
(W.H.K.L.)

Institute of Earth Sciences
Academia Sinica
P.O. Box 1-55
Nankang Taipei 115 Taiwan
(C.J.L., C.C.L.)

Manuscript received 30 July 2008